Journal of Energy Chemistry 63 (2021) 385–390

Contents lists available at ScienceDirect

Journal of Energy Chemistry

journal homepage: www.elsevier.com/locate/jechem

http://www.journals.elsevier.com/journal-of-energy-chemistry/

Dedicated to the 100th anniversary of Chemistry at Nankai University

# Development of $Sn^{2+}$-based oxyfluoride photocatalyst with visible light response of ca. 650 nm via strengthened hybridization of Sn 5*s* and O 2*p* orbitals

Yanpei Luo [a,b,1], Xin Zhou [c,1], Jiangwei Zhang [a], Yu Qi [a], Zheng Li [a], Fuxiang Zhang [a,*], Can Li [a,*]

[a] State Key Laboratory of Catalysis, Dalian Institute of Chemical Physics, Chinese Academy of Sciences, Dalian National Laboratory for Clean Energy, The Collaborative Innovation Center of Chemistry for Energy Materials (iChEM), Dalian 116023, Liaoning, China
[b] University of Chinese Academy of Sciences, Beijing 100049, China
[c] College of Environment and Chemical Engineering, Dalian University, Dalian 116622, Liaoning, China

ARTICLE INFO

*Article history:*
Received 14 June 2021
Revised 23 July 2021
Accepted 31 July 2021
Available online 9 August 2021

*Keywords:*
Photocatalyst
Visible light
Water splitting
DFT
Structural characterizations

ABSTRACT

The hybridization between the outmost *s* orbitals of metal ($Bi^{3+}$, $Sn^{2+}$, $Pb^{2+}$, $Ag^{+}$) and O 2*p* orbitals has been widely employed to develop innovative semiconductors with upshift valence band as well as extended visible light response, but it is still challenging to obtain photocatalyst with absorption edge of above 550 nm. Here we report a novel $Sn^{2+}$-based oxyfluoride $Sn_2TiNbO_6F$ (STNOF) photocatalyst with a pyrochlore structure to exhibit an extended absorption edge to 650 nm and dual functionalities of both water reduction and oxidation. Density functional theory calculations suggest that the unprecedented broad-spectrum response of STNOF is mainly ascribed to the strengthened hybridization between O 2*p* and Sn 5*s* orbitals remarkably upshifting the valence band, which is caused by the distortion and compressive strain in the $SnO_6F_2$ dodecahedron with second-order Jahn-Teller effect due to partial fluorine substitution. The structural distortion and compressive strain are experimentally confirmed by the Fourier-transformed extended X-ray absorption fine spectra. As probe tests of the photocatalytic functionalities, water reduction and oxidation half reactions were examined to see obvious $H_2$ and $O_2$ evolution under visible light irradiation. This work may provide an alternative strategy of developing extended visible light responsive semiconductors for promising solar energy conversion.



## 1. Introduction

Semiconductor photocatalysis is considered to be one of the most promising technologies to convert intermittent solar energy into storable chemical fuels from reactions like water splitting, carbon dioxide reduction, nitrogen fixation, etc. [1–8]. To efficiently convert solar energy and drive these thermodynamically unfavorable reactions, it is imperative to develop photocatalytic materials with narrow band gap while meeting the requirements of the corresponding redox potential [9–13]. Considering the fact that the valence bands of conventional metal oxide photocatalysts are mainly determined by O 2*p* orbitals, which are far more positive than the oxidation potential of water, valence band engineering represents an effective strategy to minimize the band gap and develop new visible-light-responsive photocatalysts.

Over the past few decades, construction of anions-mixed photocatalysts such as nitrogen-doped oxides [14–17], oxynitrides [18–20], oxysulfides [21–23], and oxyhalides [24–26] to elevate the valence band has attracted great attention. The visible light response of these photocatalysts is realized by introducing less negatively charged anions ($N^{3-}$, $S^{2-}$, $Cl^{-}$, $Br^{-}$, etc.) with the orbitals above O 2*p* orbitals, resulting in a reduced band gap without obviously affecting the conduction position. Apart from introducing mixed anions to modulate the valence band, another alternative approach is to combine the metals' orbitals in $s^2d^{10}$ electron configuration, such as Sn 5*s* in $Sn^{2+}$, Pb 6*s* in $Pb^{2+}$, and Bi 6*s* in $Bi^{3+}$, with the O 2*p* orbitals [26–30]. Non-centrosymmetric oxides containing both $d^0$ transition metals ($Ti^{4+}$, $Nb^{5+}$, $V^{5+}$, $W^{6+}$, etc.) and lone pair cations ($Sn^{2+}$, $Pb^{2+}$, etc.) are well-known representatives. Among them, the $Sn^{2+}$-based photocatalysts have drawn one of the most particular attentions because of its cheapness, abundance and environmentally friendliness. To date, continuous efforts have been made to explore innovative $Sn^{2+}$-based visible-light-

* Corresponding authors.
*E-mail addresses:* fxzhang@dicp.ac.cn (F. Zhang), canli@dicp.ac.cn (C. Li).
[1] These authors contributed equally to this work.

https://doi.org/10.1016/j.jechem.2021.07.028

responsive photocatalyst for promising solar water splitting, but their absorbance edges are still limited to below 550 nm [27,31]. However, to target the efficient conversion of solar to chemical energy, the ideal candidate photocatalyst was suggested to harvest the solar light of beyond and around 600 nm and to have functionalities of both reduction and oxidation [9,10]. Accordingly, it is highly desirable to develop new strategy to prepare novel $Sn^{2+}$-based photocatalysts with continuously extended the visible light response.

Recently, strain effect has been widely discussed to affect the charge separation and surface adsorption/reaction [32,33]. For example, Huang et al. reported that the enhanced strain greatly facilitates charge separation as well as molecular oxygen activation on $BiOIO_3$ [34]. Zhang et al. demonstrated that the compressive strain in ultrathin CuCr nanosheets of layered-double-hydroxide is favorable for $N_2$ chemical adsorption and $NH_3$ synthesis [35]. It is general to know that the strain of one compound is related to the symmetry of its unit cell which can be modulated via introducing extraneous metal ions or creation of defect sites [36,37]. For this purpose, introduction of $F^-$ ions with strong electronegativity should be one of the most promising ways to modulate the structural strain. Furthermore, the existence of structural strain caused by changed symmetry of unit cell in one compound is reasonably expected to change the orbital hybridization extent of atoms composed of the valence/conduction bands. It means that the strain effect should make a remarkable effect on the contribution of center-metal ions to the valence/conduction bands to cause change of light absorption edge. To our knowledge, however, the effect of strain on the light absorption has not been reported yet.

In this work, we demonstrate feasibility of substitution of fluorine to oxygen atoms in modulating the structural strain and narrowing the band gap of $Sn^{2+}$-based oxide, based on which a novel STNOF photocatalyst with an unprecedentedly extended absorption edge of ca. 650 nm can be synthesized. Density functional theory (DFT) calculations reveal that the valence band maximum of $Sn_2TiNbO_6F$ (STNOF) is mainly composed of O 2*p* and Sn 5*s* states, whose orbital hybridization can be strengthened by the substitution of fluorine. Structural simulation and extended X-ray absorption fine structure (EXAFS) reveal that the fluorine substitution to part oxygen atoms will enhance the distortion of the $SnO_6F_2$ dodecahedron to produce compressive strain, giving rise to the strengthened Sn 5*s* and O 2*p* hybridization.

## 2. Results and discussion

As seen in Fig. 1(a), STNOF is of an $A_2B_2X_6X'$-type pyrochlore structure (space group: $Fd\bar{3}m$) with two distinct anion sites, among which the X site is occupied by the oxygen anion while the X′ site is occupied by the fluoride anion. The compound skeleton is composed of corner-sharing $TiO_6$ or $NbO_6$ octahedron and F-Sn-F chains. STNOF was synthesized through a solid-state reaction using a stoichiometric mixture of SnO, $SnF_2$, $TiO_2$ and $Nb_2O_5$ at the temperature of 973 K for 10 h in the sealed corundum tube with filled argon gas. Fig. 1(b) shows the typical X-ray diffraction (XRD) patterns of a single-phase of STNOF, in which all the peaks can be indexed with the PDF-04-001-8271 and no extra peaks belonging to any impurities can be obviously observed. The scanning electron microscope (SEM) image (inset, Fig. 1b) indicates that the prepared STNOF has a particle size distribution in the range of 1 to 10 μm. This result is consistent with relatively low specific surface area of 0.6 $m^2\ g^{-1}$ measured through the BET method. Energy-dispersive spectroscopy (EDS) mapping analysis confirms the coexistence of Sn, Ti, Nb, O and F elements and homogeneous distribution (Figs. S1 and S2). In particular, the spatial distributions of fluorine in STNOF have also been investigated by X-ray photoelectron spectroscopy (XPS) under different time of $Ar^+$ sputtering. As shown in Fig. S3, the intensity of F 1*s* XPS peak at 684.8 eV is not obviously changed from the surface to the bulk phase, well indicating that the $F^-$ ions have been uniformly substituted instead of just on the surface. XPS spectra containing Sn 3*d*, Ti 2*p*, Nb 3*d* and O 1*s* were also studied to further understand the electronic structure of STNOF (Fig. S4), based on which the valence states of the constituent elements are known to be in a good accordance with the formula, $Sn_2(II)Ti(IV)Nb(V)O_6(II)F(I)$. Furthermore, the oxidation state of Sn ions in STNOF was characterized by the X-ray absorption near edge structure (XANES), during which the $Sn_2Nb_2O_7$ (donated as SNO) and SnO oxides free of fluorine atoms were employed as references for discussion. As shown in Fig. S5, the Sn *K*-edge of XANES in the STNOF and SNO sample exhibit a very similar near-edge structure as SnO, further demonstrating their similar valence ($Sn^{2+}$) in accordance with results of the above XPS analysis.

Fig. 1(c) gives the typical ultraviolet–visible diffuse reflectance spectroscopy (UV–Vis DRS) of STNOF, from which the absorption edge of STNOF can be deduced to be ca. 650 nm, as is well consistent with the red color of the material (inset, Fig. 1c). The band gap of STNOF estimated from the tauc plot (Fig. S6) is about 1.88 eV, which is much smaller than that of some typical $Sn^{2+}$-based narrow bandgap semiconductors such as $SnNb_2O_6$ (2.3 eV) or $Sn_2Nb_2O_7$ (2.3 eV). As seen in Fig. 1(d), both VBM and CBM obtaining from the DFT calculation and simulation are situated at the Gamma (G) point, indicating that the STNOF is featured as direct band gap semiconductor. As demonstrated by Mott-Schottky (M-S) plot given in Fig. 1(e), the STNOF is an n-type semiconductor with the flat band potential of ca. − 0.07 V (versus reversible hydrogen electrode). It is interesting to note that the flat band position is not obviously affected by the pH environment, which may attribute to the small acid dissociation constant of hydroxyl groups on STNOF as similar to $Sm_2Ti_2S_2O_5$ (Fig. S7) [23]. It is well-known that the bottom of conduction bands of n-type semiconductors is about 0.1 V more negative than the flat band potential [38], so the conduction band position of STNOF can be proposed to be about − 0.17 V. Given that the bandgap of STNOF is 1.88 eV, the valence band position is proposed to be 1.71 eV, which can be further verified by the ultraviolet photoelectron spectroscopy (UPS) measurements in Fig. S8. The valence band maximum position was determined to be − 6.29 eV compare with the vacuum level corresponding to the 1.79 eV (versus reversible hydrogen electrode). Based on above discussion, Fig. 1(f) gives a schematic illustration on the band positions of STNOF, where both the conduction and valence band of STNOF are thermodynamically feasible for reduction of water (or $CO_2$, $N_2$) and water oxidation, respectively. It means that the STNOF developed here is highly promising for most solar-to-chemical energy conversion reactions.

In order to get insight into the widely extended visible light absorption, DFT simulation was calculated. As shown in Fig. 2(a), the valence band maximum of STNOF is mainly composed of O 2*p* states with non-negligible contributions from Sn 5*s* states, whereas the conduction band minimum is mostly comprised of Ti 3*d*, mixed with Nb 4*d*, Sn 5*p* and O 2*p* states. An enlarged view of the partial DOS of STNOF from − 1.5 to 1 eV was shown in Fig. S9. It should be pointed out that the charge negativity of $F^-$ ions is stronger than that of $O^{2-}$ ions, so the hybridization of F 2*p* and O 2*p* is unfavorable for the upshift of valence band. The calculated band gap of STNOF is 0.75 eV, which is smaller than the experimental value due to the limitation of GGA-PBE method [39]. The O 2*p* orbital and Sn 5*s* orbital have strong hybridization at the bottom (from − 9 to − 8 eV) and top (from − 2 to − 1 eV) of the valence band. This phenomenon is similarly observed in SnO and PbO with $s^2$ lone pair, which can be attributed to the revised lone pair (RLP) mechanism [40]. The antibonding orbitals

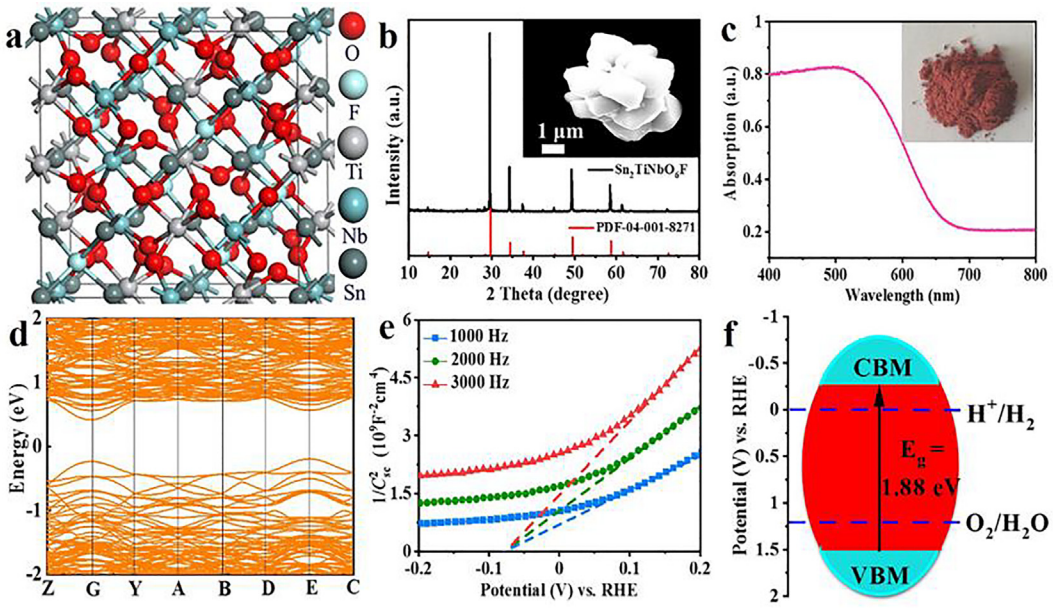


**Fig 1.** Structural simulation and characterizations of STNOF. (a) Crystal structure (space group: $Fd\bar{3}m$); (b) XRD patterns, and SEM image (inset); (c) UV–Vis DRS, and a picture of STNOF (inset); (d) the simulated band structure; (e) Mott-Schottky plot; (f) schematic diagram of the estimated band positions (CBM: conduction band maximum, VBM: valence band minimun, $E_g$: band gap).

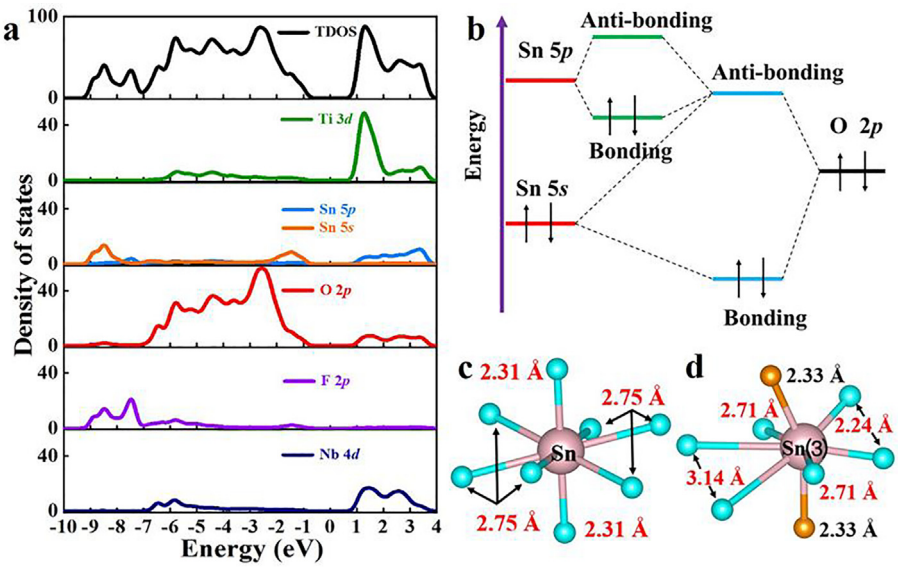


**Fig. 2.** DFT simulations of STNOF and illustration of the orbital interactions in STNOF. (a) DOS plot of STNOF; (b) illustration of the orbital interactions between Sn 5*s* and O 2*p* in STNOF; (c and d) the local coordination environments around Sn atom in SNO and STNOF (Sn-3).

formed by Sn 5*s* and O 2*p* orbitals are stabilized by hybridization with the unoccupied Sn 5*p* orbitals, resulting in upward shift of the O 2*p* orbitals in STNOF (see Fig. 2b). The tendency to form a strong hybridization is therefore closely related to the energy difference between the cation *s* states and the anion *p* states [41]. If this difference is large, the formation of the bonding orbital is less favorable, and thus the hybridization is not obvious. It should be noted that among the common oxides containing heavy metal (i.e. Sn, Pb, Bi) with $s^2$ lone pair, the strongest *s*-*p* orbital hybridization is expected to happen between Sn 5*s* and O 2*p* where $\Delta E_{s\text{-}p}$ = 1.4 eV [40].

The hybridization of Sn 5*p* states with the antibonding states of Sn 5*s* and O 2*p* is predominantly determined by the crystal distortion, which can be strengthened by the second-order Jahn-Teller (SOJT) effect [42,43]. Normally, without crystal distortion, the hybridization of Sn 5*p* with the antibonding states of Sn 5*s* and O 2*p* will become impossible. And the stronger the hybridization extent is, much larger the extended extent of visible light absorption is [24]. As far as STNOF is concerned, the part substitution of oxygen by fluorine atoms with stronger negativity is expected to make the second-order Jahn-Teller effect to cause strengthened crystal disorder and compressive strain, resulting in stabilization of the anti-bonding orbital between Sn 5*s* and O 2*p* as well as greatly extended visible light absorption.

In order to confirm the existence of crystal disorder and compressive strain, the local coordination environment around Sn atoms in SNO and STNOF is first compared by structural simulations. As seen in Figs. 2(c and d), the SNO have two short Sn–O

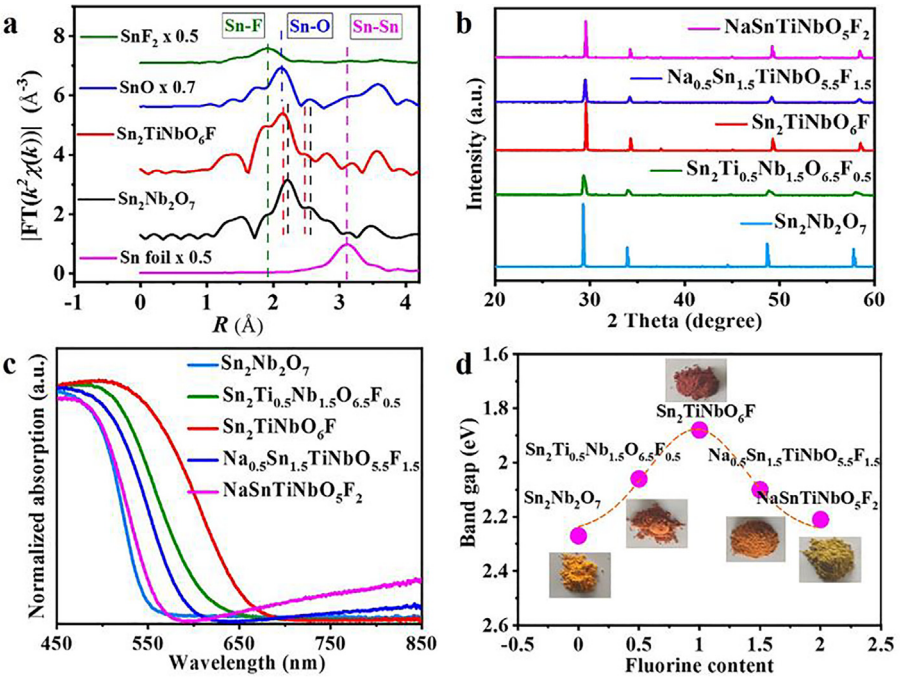


**Fig. 3.** (a) Sn *K*-edge EXAFS spectra of STNOF with Sn foil, SnO, $SnF_2$ and SNO employed as references. Characterizations of a series of $Sn^{2+}$-based oxyfluoride compounds: (b) XRD patterns; (c) UV-Vis diffuse reflectance spectrum; (d) variation of band gap as a function of fluorine content (inset: pictures of samples).

bonds (2.31 Å) and six long Sn–O bonds (2.75 Å), while STNOF have four kinds of Sn atoms with different coordination environment (Fig. S10). For example, Sn 3 in STNOF have two shortest Sn–O bonds (2.24 Å) and two longest Sn–O bonds (3.14 Å) in the opposite direction. On the basis of this structure, it clearly shows the lattice distortion in the dodecahedron is enhanced by the SOJT effect. Moreover, since the STNOF and SNO have the same pyrochlore structure, the different Sn–O bond length reflects the existence of crystal distortion and compressive strain to some extent [44]. And the shortest Sn–O bond length in STNOF (2.24 Å) is shorter than that in SNO (2.31 Å), so the compressive strain that causes lattice distortion in STNOF is relatively large.

Secondly, X-ray absorption fine spectra spectroscopy (XAFS) was used to experimentally probe the coordination environment around the Sn atoms in STNOF and SNO for its high sensibility [45,46]. The Fourier-transformed (FT) EXAFS spectra for STNOF and SNO are shown in Fig. 3(a) and the extracted structural parameters are listed in Table S1. STNOF exhibits a major peak at 2.14 Å, attributed to the shortest Sn–O bonds of first Sn–O shell in STNOF, which is shorter than that in SNO (2.21 Å). This is the direct evidence for the existence of compressive strain in the crystal, which is consistent with the theoretical calculation results. The peaks at 1.87 and 2.45 Å derived from STNOF can be assigned to the Sn–F bonds and other longer Sn–O bonds in first Sn–O shell, while SNO have a minor peak at 2.56 Å corresponding to six long Sn–O bonds. Furthermore, the reduced coordination number (4.0) for Sn–O bonds in STNOF compared to SNO (6.0) demonstrates the partial substitution of fluorine to oxygen (Table S1). It should be mentioned that the intensity of peak is not only related to the number, but also to the distance [42,43]. As seen in Table S1, the distance of Sn–O bonds with a coordination number of 2 is shorter than that of Sn–O bonds with a coordination number of 6 or 4. In this case, the shorter bond distance causes enhanced intensity peak to a certain extent, leading to observation of higher peak intensity of the Sn–O with coordination number of 2 than that of 4 or 6. These results provide solid experimental evidence for a structural compression and support the conclusion that the fluorine partial substitution will change crystal symmetry to produce compressive strain. All of them should be responsible for the distinct observation that most of previous $Sn^{2+}$-based photocatalysts can only absorb visible light of below 550 nm, while the STNOF developed in this work can absorb visible light up to 650 nm.

In order to verify the universality of the fluorine substitution strategy, a series of $Sn^{2+}$-based oxyfluoride compounds with different fluorine content were synthesized. It is worth noting that these $Sn^{2+}$-based oxyfluoride compounds obtained by partial substitution of A-sites and B-sites atoms still retain the pyrochlore structure, whose XRD and UV–Vis DRS patterns are shown in Fig. 3(b and c). It should be mentioned that the partial substitution of $O^{2-}$ by $F^-$ in lattice sites of $Sn_2Ti_{0.5}Nb_{1.5}O_{6.5}F_{0.5}$ photocatalyst will induce the lattice shrinkage to cause the shift of the (222) reflection peak to higher $2\theta$ angles (Fig. S11), well revealing the existence of lattice strain. The band gaps of as-obtained oxyfluoride semiconductors decrease initially on incorporation of fluorine up to a concentration above which the band gaps increase, showing a volcanic curve in Fig. 3(d). The volcano apex corresponds to STNOF where fluorine atoms completely replace oxygen atoms in O′-site of $A_2B_2O_6O'$-type pyrochlore. It should be pointed out that the substitution of $Ti^{4+}$ to $Nb^{5+}$ here is mainly used for charge balance, and the Ti 3*d* orbital makes an obvious contribution to the conduction band (Fig. S9). It has been reported that the displacement of A-site ion in the pyrochlore structure may weaken the hybridization between heavy metal n*s* and O 2*p* orbitals, while the partial substitution of O-site ion in $A_2B_2O_6O'$ by fluorine may enhance the hybridization [22]. In these $Sn^{2+}$-based oxyfluoride compounds, the hybridization shows a weakened trend through displacing A-site ion, and the reason need to be further studied. Anyway, the fluorine substitution is supposed to be an effective and universe strategy of adjusting the band gap of oxides containing $d^0$ transition metals with lone pair electron.

To evaluate the functionalities of the as-obtained STNOF, the water splitting performances were thus examined as the probe tests. Photoreduction functionality was first examined by water reduction conducted in the aqueous solution containing tri-

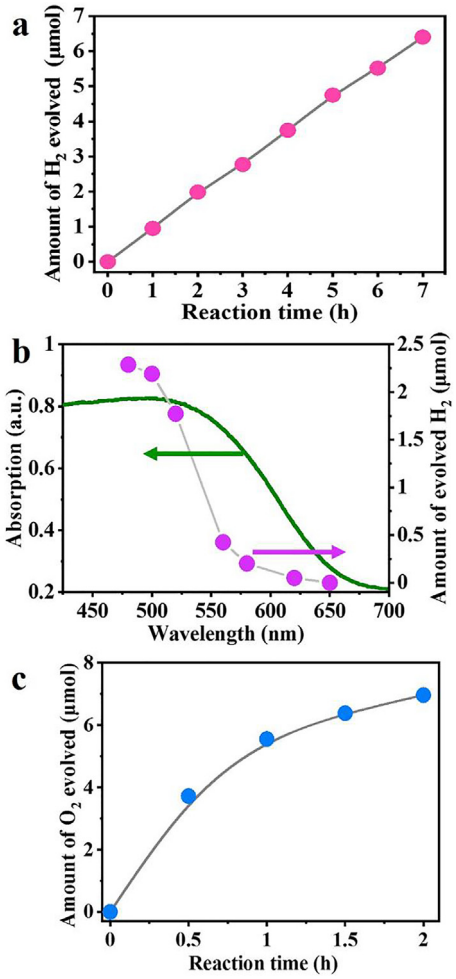


**Fig. 4.** Photocatalytic performances of water reduction or oxidation on STNOF. (a) Time course curve of photocatalytic $H_2$ evolution. Reaction conditions: 0.15 g 0.5 wt % Pt/STNOF; 120 mL $H_2O$; 30 mL TEOA; 300 W Xe lamp ($I$ = 15 A; $\lambda \geq 420$ nm). (b) Photocatalytic $H_2$ evolution rate as a function of the cutoff wavelength of incident light (pink circles). Reaction conditions: 0.15 g 0.5 wt% Pt/STNOF; 120 mL $H_2O$; 30 mL TEOA; 300 W Xe lamp ($I$ = 20 A). (c) Time course curve of photocatalytic $O_2$ evolution. Reaction conditions: 0.15 g 1 wt% $CoO_x$/STNOF; 150 mL 10 mM $AgNO_3$ aqueous solution; 300 W Xe lamp ($I$ = 15 A; $\lambda \geq 420$ nm).

ethanolamine (TEOA) as sacrificial agents. Meanwhile, platinum nanoparticles were photo-deposited as cocatalyst [47,48]. As seen in Fig. 4(a), stable $H_2$ evolution can be observed under visible light ($\lambda \geq 420$ nm) and the hydrogen evolution activity of Pt/STNOF displayed almost no decay within three cycles (Fig. S12), demonstrating the photochemical stability of STNOF in the experimental region. The apparent quantum efficiency (AQE) of the STNOF photocatalyst has been measured to be about 0.05% under the irradiation of 420 ± 10 nm. Moreover, the trend of hydrogen evolution activity is in good accordance with that of UV–Vis DRS (Fig. 4b), indicating that the hydrogen evolution reaction is a light-driven catalytic reaction. On the other hand, its photo-oxidation functionality was examined via the water oxidation performed in the aqueous solution containing 10 mM $AgNO_3$ under visible light, during which $CoO_x$ nanoparticles were impregnated as the cocatalyst. As given in Fig. 4(c), the obviously observed $O_2$ evolution well demonstrates its oxidation functionality. It should be pointed out that the slight decrease in the activity curve as a function of reaction time should result from the light absorption competition of the deposited silver, as similarly observed in most of previous literatures [49,50]. It is worth noting that no $H_2$ or $O_2$ can be detected in the experimental region if no catalysts, TEOA or Pt was added or under dark (Tables S2 and S3). Additionally, free of $CoO_x$ the photocatalytic $O_2$ evolution rate is obviously decreased, demonstrating importance of cocatalyst. What's more, the photocatalysts before and after reactions exhibit no obvious change in the XRD patterns and XPS spectra (Figs. S13 and S14), further demonstrating its photochemical stability. By virtue of the dual functionalities, the STNOF developed here is expected to be a good candidate photocatalyst for promising overall water splitting, towards which innovative preparation methodologies and surface/interface modulation strategies should be further investigated to enhance its activities [51]. It should be pointed out that the finding of functionalities for one novel photocatalyst is more important than its activities because of the fact that many novel photocatalysts show extremely low activities at its first report as given Table S4, but which can be continuously improved by various modification strategies like the $C_3N_4$ photocatalyst [52]. However, the functionalities are normally not easily modified because of both thermodynamic and/or kinetics challenges.

## 3. Conclusions

Here we developed a $Sn^{2+}$-based oxyfluoride photocatalyst STNOF via simple solid-state reaction, which can not only absorb light with wide spectrum up to 650 nm, but also can drive both water reduction and oxidation reaction under visible light irradiation. The unprecedented broad-spectrum response of $Sn_2TiNbO_6F$ is proposed to arise from the strengthened hybridization between O 2*p* and Sn 5*s* orbitals caused by the distortion and compressive strain of the $SnO_6F_2$ dodecahedron due to the fluorine substitution. To our knowledge, the STNOF reported here should be the first $Sn^{2+}$-based semiconductor with absorption edge beyond 600 nm and dual functionalities of both photocatalytic reduction and oxidation. It is worth noting that the substitution of oxygen atoms by fluorine atoms with higher electronegativity is not favorable to extend the visible light absorption by itself, but here we demonstrate the feasibility of part substitution of fluorine to oxygen atoms in extending visible light absorption via distortion of the $SnO_6F_2$ dodecahedron to produce compressive strain and strengthened hybridization between O 2*p* and Sn 5*s* orbitals. Interestingly, the expansion of visible light absorption can be observed in other $Sn^{2+}$-based oxyfluoride compounds with different fluorine content, demonstrating its university. Our results demonstrate effectiveness of extending visible light absorption via modulating compressive strain of unit cell, as is expected to be an alternative strategy to develop more broad-spectrum responsive semiconductors for promising solar energy conversion.

## Declaration of Competing Interest

The authors declare that they have no known competing financial interests or personal relationships that could have appeared to influence the work reported in this paper.

## Acknowledgments

This work was conducted by the Fundamental Research Center of Artificial Photosynthesis (FReCAP), financially supported by the National Natural Science Foundation of China (NSFC) (22088102). This work was also supported by the National Natural Science Foundation of China (21633009, 21633010, 21925206), the Cooperation Fund of Dalian National Laboratory for Clean Energy (DNL 201913), International Partnership Program of Chinese Academy of Sciences (121421KYSB20190025), the DICP foundation of innovative research (DICP I201927) and Strategic Priority Research Pro-

gram of Chinese Academy of Sciences (XDB17000000). F. Zhang thanks the support from Liaoning Revitalization Talents Program (XLYC1807241).

## Appendix A. Supplementary data

Supplementary data to this article can be found online at https://doi.org/10.1016/j.jechem.2021.07.028.

## References

[1] Q. Wang, K. Domen, Chem. Rev. 120 (2020) 919–985.
[2] A. Kudo, Y. Miseki, Chem. Soc. Rev. 38 (2009) 253–278.
[3] T. Kong, Y. Jiang, Y. Xiong, Chem. Soc. Rev. 49 (2020) 6579–6591.
[4] S. Wang, F. Ichihara, H. Pang, H. Chen, J. Ye, Adv. Funct. Mater. 28 (2018) 1803309.
[5] J. White, M. Baruch, J. Pander, Y. Hu, I. Fortmeyer, J. Park, T. Zhang, K. Liao, J. Gu, Y. Yan, T. Shaw, E. Abelev, A. Bocarsly, Chem. Rev. 115 (2015) 12888–12935.
[6] T. Xu, J. Liang, S. Li, Z. Xu, L. Yue, T. Li, Y. Luo, Q. Liu, X. Shi, A. Asiri, C. Yang, X. Sun, Small Sci. 1 (2021) 2000069.
[7] S. Wang, X. Han, Y. Zhang, N. Tian, T. Ma, H. Huang, Small Sci. 2 (2020) 2000061.
[8] L. Liu, H. Huang, Z. Chen, H. Yu, K. Wang, J. Huang, H. Yu, Y. Zhang, Angew. Chem. Int. Ed. 133 (2021) 2–8.
[9] S. Chen, T. Takata, K. Domen, Nat. Rev. Mater. 2 (2017) 17050.
[10] K. Maeda, K. Domen, J. Phys. Chem. Lett. 1 (2010) 2655–2661.
[11] Y. Wang, X. Wang, M. Antonietti, Angew. Chem. Int. Ed. 51 (2012) 68–89.
[12] J. Cui, C. Li, F. Zhang, ChemSusChem. 12 (2019) 1872–1888.
[13] X. Li, Z. Wang, L. Wang, Small Sci. 1 (2021) 2000074.
[14] R. Asahi, T. Morikawa, H. Irie, T. Ohwaki, Chem. Rev. 114 (2014) 9824–9852.
[15] R. Asahi, T. Morikawa, T. Ohwaki, K. Aoki, Y. Taga, Science 293 (2001) 269–271.
[16] G. Liu, L. Yin, J. Wang, P. Niu, C. Zhen, Y. Xie, H. Cheng, Energy Environ. Sci. 5 (2012) 9603–9610.
[17] J. Cui, T. Liu, Y. Qi, D. Zhao, M. Jia, G. Liu, F. Zhang, C. Li, J. Mater. Chem. A 5 (2017) 18870–18877.
[18] K. Maeda, K. Domen, J. Phys. Chem. C 111 (2007) 7851–7861.
[19] C. Pan, T. Takata, M. Nakabayashi, T. Matsumoto, N. Shibata, Y. Ikuhara, K. Domen, Angew. Chem. Int. Ed. 54 (2015) 2955–2959.
[20] K. Maeda, T. Takata, M. Hara, N. Saito, Y. Inoue, H. Kobayashi, K. Domen, J. Am. Chem. Soc. 127 (2005) 8286–8287.
[21] Y. Goto, J. Seo, K. Kumamoto, T. Hisatomi, Y. Mizuguchi, Y. Kamihara, M. Katayama, T. Minegishi, K. Domen, Inorg. Chem. 55 (2016) 3674–3679.
[22] V. Meignen, L. Cario, A. Lafond, Y. Moëlo, C. Guillot-Deudon, A. Meerschaut, J. Solid State Chem. 177 (2004) 2810–2817.
[23] A. Ishikawa, T. Takata, J. Kondo, M. Hara, H. Kobayashi, K. Domen, J. Am. Chem. Soc. 124 (2002) 13547–13553.
[24] R. Kuriki, T. Ichibha, K. Hongo, D. Lu, R. Maezono, H. Kageyama, O. Ishitani, K. Oka, K. Maeda, J. Am. Chem. Soc. 140 (2018) 6648–6655.
[25] K. Oka, H. Hojo, M. Azuma, K. Oh-ishi, Chem. Mater. 28 (2016) 5554–5559.
[26] D. Kato, K. Hongo, R. Maezono, M. Higashi, H. Kunioku, M. Yabuuchi, H. Suzuki, H. Okajima, C. Zhong, K. Nakano, R. Abe, H. Kageyama, J. Am. Chem. Soc. 139 (2017) 18725–18731.
[27] D. Noureldine, K. Takanabe, Catal. Sci. Technol. 6 (2016) 7656–7668.
[28] H. Kim, D. Hwang, J. Lee, J. Am. Chem. Soc. 126 (2004) 8912–8913.
[29] A. Kudo, K. Ueda, H. Kato, I. Mikami, Catal. Lett. 53 (1998) 229–230.
[30] T. Chen, L. Liu, C. Hu, H. Huang, Chinese. J. Catal. 42 (2021) 1413–1438.
[31] Y. Hosogi, Y. Shimodaira, H. Kato, H. Kobayashi, A. Kudo, Chem. Mater. 20 (2008) 1299–1307.
[32] S. Tu, Y. Guo, Y. Zhang, C. Hu, T. Zhang, T. Ma, H. Huang, Adv. Funct. Mater. 30 (2020) 2005158.
[33] F. Chen, H. Huang, L. Guo, Y. Zhang, T. Ma, Angew. Chem. Int. Ed. 58 (2019) 10061–10073.
[34] H. Huang, S. Tu, C. Zeng, T. Zhang, A. Reshak, Y. Zhang, Angew. Chem. Int. Ed. 56 (2017) 11860–11864.
[35] Y. Zhao, Y. Zhao, G. Waterhouse, L. Zheng, X. Cao, F. Teng, L. Wu, C. Tung, D. O'Hare, T. Zhang, Adv. Mater. 29 (2017) 1703828.
[36] G. Shi, Y. Wang, F. Zhang, B. Zhang, Z. Yang, X. Hou, S. Pan, K. Poeppelmeier, J. Am. Chem. Soc. 139 (2017) 10645–10648.
[37] H. Wu, H. Yu, Z. Yang, X. Hou, X. Su, S. Pan, K. Poeppelmeier, J. Rondinelli, J. Am. Chem. Soc. 135 (2013) 4215–4218.
[38] Y. Matsumoto, J. Solid State Chem. 126 (1996) 227–234.
[39] J. Perdew, K. Burke, M. Ernzerhof, Phys. Rev. Lett. 77 (1996) 3865–3868.
[40] A. Walsh, D. Payne, R. Egdell, G. Watson, Chem. Soc. Rev. 40 (2011) 4455–4463.
[41] K. Tolborg, C. Gatti, B. Iversen, IUCrJ. 7 (2020) 480–489.
[42] S. Oh, W. Dong, M. Kang, Dalton. Trans. 41 (2012) 2995–3000.
[43] P. Halasyamani, Chem. Mater. 16 (2004) 3586–3592.
[44] H. Wakayama, K. Utimula, T. Ichibha, R. Kuriki, K. Hongo, R. Maezono, K. Oka, K. Maeda, J. Phys. Chem. C. 122 (2018) 26506–26511.
[45] H. Fei, J. Dong, Y. Feng, C. Allen, C. Wan, B. Volosskiy, M. Li, Z. Zhao, Y. Wang, H. Sun, P. An, W. Chen, Z. Guo, C. Lee, D. Chen, I. Shakir, M. Liu, T. Hu, Y. Li, A. Kirkland, X. Duan, Y. Huang, Nat. Catal. 1 (2018) 63–72.
[46] J. Guan, Z. Duan, F. Zhang, S. Kelly, R. Si, M. Dupuis, Q. Huang, J. Chen, C. Tang, C. Li, Nat. Catal. 1 (2018) 870–877.
[47] J. Lian, D. Li, Y. Qi, N. Yang, R. Zhang, T. Xie, N. Guan, L. Li, F. Zhang, J. Energy Chem. 55 (2021) 444–448.
[48] J. Yang, D. Wang, H. Han, C. Li, Acc. Chem. Res. 46 (2013) 1900–1909.
[49] H. Kunioku, M. Higashi, O. Tomita, M. Yabuuchi, D. Kato, H. Fujito, H. Kageyama, R. Abe, J. Mater. Chem. A. 6 (2018) 3100–3107.
[50] L. Wan, F. Xiong, B. Zhang, R. Che, Y. Li, M. Yang, J. Energy Chem. 27 (2018) 367–371.
[51] S. Chen, Y. Qi, C. Li, K. Domen, F. Zhang, Joule. 2 (2018) 2260–2288.
[52] L. Lin, Z. Yu, X. Wang, Angew. Chem. Int. Ed. 58 (2019) 6164–6175.